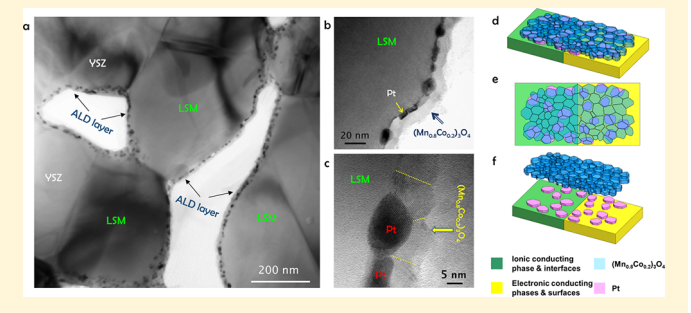


# Conformal Electrocatalytic Surface Nanoionics for Accelerating High-Temperature Electrochemical Reactions in Solid Oxide Fuel Cells

Yun Chen,<sup>†</sup> Kirk Gerdes,<sup>‡</sup> Sergio A. Paredes Navia,<sup>†</sup> Liang Liang,<sup>†</sup> Alec Hinerman,<sup>†</sup> and Xueyan Song\*,<sup>†</sup>

Supporting Information

ABSTRACT: Additive implantation of electrocatalysts onto the internal surface of porous cathodes holds great promise to accelerate the electrochemical reactions within solid oxide fuel cells (SOFCs). Here we utilize atomic layer deposition (ALD) to apply dual catalysts with (Mn<sub>0.8</sub>Co<sub>0.2</sub>)<sub>3</sub>O<sub>4</sub> and a minute amount of Pt on the cathode consisting of lanthanum strontium manganite (LSM) and yttria-stabilized zirconia (YSZ). Coating this material with optimum ALD layer thickness resulted in a 53% reduction of polarization resistance and a 350% SOFC peak power density enhancement at 750 °C. During the electrochemical operations, the



dual catalysts interact synergistically and evolve into superjacent conformal electrocatalytic  $(Mn_{0.8}Co_{0.2})_3O_4$  nanoionics with high-density grain boundaries and subjacent discrete nano Pt particles evenly distributed on both the LSM and YSZ. The configuration consequently extends the active electrochemical reaction sites to the entire internal surface of the cathode. For the first time in the field of SOFCs, the present work demonstrates the formation of the electrocatalytic surface nanoionics and its resultant accelerated mass and charge transfer to dramatically boost the cell performance.

KEYWORDS: Solid oxide fuel cell, cathode, atomic layer deposition, dual catalyst, eletrocatalytic nanoionics

Solid oxide fuel cells (SOFCs) offer excellent fuel flexibility and high energy conversion efficiency for power generation. 1-4 In comparison with the emerging protonic conducting SOFCs 5,6 that still face challenges to be commercialized, conventional SOFCs with oxygen ionic conducting electrolyte are proven to be stable over several thousand hours of operation and are commercially available. Energy systems based on the reversible SOFC operated in both fuel cell and electrolysis modes are also feasible. For the vehicles that fuel cells are already used in, the SOFCs are extremely attractive in term of the fuel flexibility, high power density, and relative tolerance toward fuel impurities.<sup>8-10</sup> Improving the power density will further expand the range of SOFC usage from stationary power generation to on-board vehicle applications. Regardless of the intense research effort during the past 20 years, the biggest polarization losses impeding the cell power density and longevity still relate to the high activation energy for the oxygen reduction reaction (ORR) in the cathode. 11 Among the various cathode materials at high temperatures over 850 °C, the lanthanum strontium manganite (LSM)-based materials are the most popular choice for SOFC, owing to their high chemical and thermal compatibility with conventional yttria-stabilized zirconia (YSZ) electrolyte, adequate electrochemical performance,

and superior stability upon long-term operation.<sup>12</sup> However, LSM possesses negligible ionic conductivity and low oxygen surface exchange and thus restricts the electrochemically active sites to the triple-phase boundaries (TPBs) where ionic and electronic conducting phases and gas-phase meet. 13,14 By contrast, cobaltite-based perovskite including lanthanum strontium cobalt ferrite (LSCF) exhibits mixed ionic and electronic conductivity, and the TPB region of LSCF cathodes is effectively expanded across the entire surface. However, LSCF is susceptible to Sr segregation 15 and presents good stability though inferior to LSM. For the practical SOFC applications, the LSM-based cathode with increased TPBs are much preferred. As such, infiltration has been developed to introduce various materials into the porous cathode. 16-20 Nevertheless, adding TPBs requires the intimate implantation of an ionic conductor on the electrocatalytic LSM surface directly and/or the addition of the electrocatalyst on the ionicconducting YSZ surface precisely. Furthermore, for those additive TPBs to be effective, the newly implanted TPBs must be dense with a spacing of <50 nm apart to form a percolating

Received: August 26, 2019
Revised: September 30, 2019
Published: October 31, 2019



<sup>&</sup>lt;sup>†</sup>Department of Mechanical and Aerospace Engineering, West Virginia University, Morgantown, West Virginia 26506, United States <sup>‡</sup>National Energy Technology Laboratory, United States Departmet of Energy, Morgantown, West Virginia 26507, United States

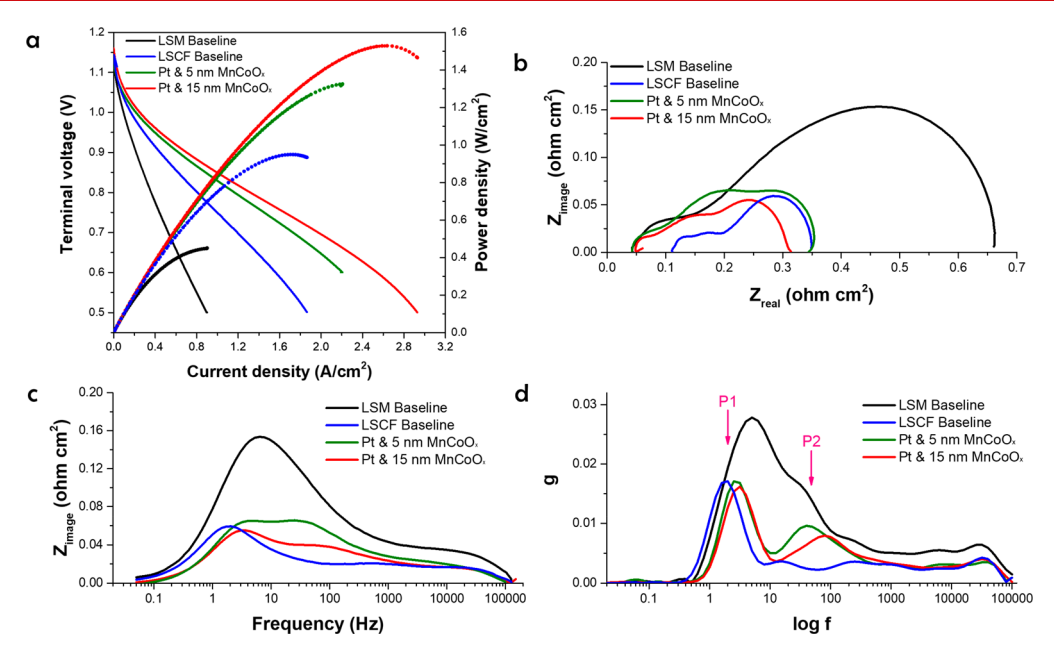


Figure 1. Electrochemical performance and impedance data for cell no. 1 LSM baseline cell, cell no. 2 LSM cell with Pt and 5 nm  $(Mn_{0.8}Co_{0.2})_3O_4$  layer, cell no. 3 the LSM cell with Pt and 15 nm  $(Mn_{0.8}Co_{0.2})_3O_4$  layer, and cell no. 4 the LSCF baseline cell. (a) Terminal voltage and power density as a function of current density for four test cells at 750 °C. (b) Nyquist plots of four cells at a constant current of 0.3 A/cm². (c) Bode plots of four cells at a constant current of 0.3 A/cm². (d) Corresponding deconvolution spectra of the impedance data collected from four cells. Two major arcs with the frequency ranging at 1–4 Hz and 10–200 Hz are indicated by  $P_1$  and  $P_2$ , respectively.

Table 1. Power Density and Resistance at 750°C for the Cells with Cathodes Having Different Surface Architecture

cell no.	backbone surface architecture	$(\Omega \text{ cm}^2)$	$(\Omega \frac{R_{\rm p}}{{ m cm}^2})$	peak power (W/cm²)	power at 0.8 V $\left(W/\text{cm}^2\right)$	peak power enhancement factor to cell no. 1	peak power enhancement factor to cell no. 4
no. 1	LSM/YSZ baseline	0.045	0.574	0.44	0.28	1	
no. 2	Pt & 5 nm $(MnCo)O_x$	0.043	0.300	1.32	0.95	3	1.4
no. 3	Pt & 15 nm $(MnCo)O_x$	0.051	0.273	1.53	1.06	3.5	1.6
no. 4	LSCF/SDC baseline	0.110	0.239	0.95	0.63		1

network during polarization. <sup>13</sup> Selective implantation of ionic conductor and electrocatalyst on LSM and YSZ surfaces separately and simultaneous introduction of high-density TPBs have been almost impossible to achieve through various solution-based infiltration. Solution-based infiltration often results in the uncontrolled distribution of infiltrated materials.

Here we present, for the first time, the  $ALD^{21-25}$  coating of the electrocatalytic  $(Mn_{0.8}Co_{0.2})_3O_4$  nanoionics and a minute amount of nano Pt to extend the ORR pathway from the originally localized TPBs to the entire internal surface of the LSM/YSZ backbone. Such coating increases the peak power density of the commercial cell by 350% and is the highest performance enhancement achieved using various infiltrations.

Results and Discussion. The present study aims to make the ALD processing of catalysts to be practical for SOFC industrial application, which requires that cells subject to ALD processing need to possess strict reproducible properties. Accordingly, commercial anode-supported cells with identical Ni/YSZ anodes are used as a baseline and subjected to further ALD coating. The performance of two ALD coated cells (no. 2 and no. 3) with LSM/YSZ cathode along with two baseline cells having LSM/YSZ (no. 1) and LSCF/samarium-doped cerium oxide (SDC) cathode (no. 4) were evaluated through electrochemical operation carried out at 750 °C in H<sub>2</sub> and air for anode and cathode, respectively. The as-deposited ALD dual-layer consists of subjacent Pt with discrete ~3 nm Pt

particles<sup>26</sup> and a superjacent  $(Mn_{0.8}Co_{0.2})_3O_4$  layer with a thickness of 5 and 15 nm for cell no. 2 and cell no. 3, respectively. The schematic of the ALD processing is shown in Figure S1. The cell performances are shown in Figure 1 and listed in Table 1.

For the baselines for cell no. 1 and cell no. 4, the peak power densities are 0.44 and 0.95 W/cm², respectively, at 750 °C, and the baseline cells of cell no. 4 with LSCF/SDC cathode are performing better. A significant power density increase (in Figure 1a) was observed from the ALD-coated cells. At 0 h operation, in comparison with the cell no. 1 340% and 380% increases in power densities at 0.8 V are achieved for cell no. 2 and cell no. 3, respectively. Meanwhile, cell no. 3 exhibits a peak power density of 1.53 W/cm² at 750 °C, which is 350% of baseline cell no. 1. To the best of our knowledge, such a 350% peak power density increase is the highest enhancement ever reported for state-of-the-art SOFCs with various infiltration. Owing to the negligible amount of ALD materials coated on the as-fabricated cells, the 350% increase is simultaneously achieved in terms of both power density and specific power.

At 0.8 V, the power density of ALD-coated LSM/YSZ cell no. 3 is 170% greater than the commercial cell with mixed conducting LSCF/SDC cathode (cell no. 4) operated under the same conditions, as shown in Figure 1a and Table 1. Cell no. 3 exhibited a slight decrease in power density over the first 24 h of operation, reaching stable performance enhancement

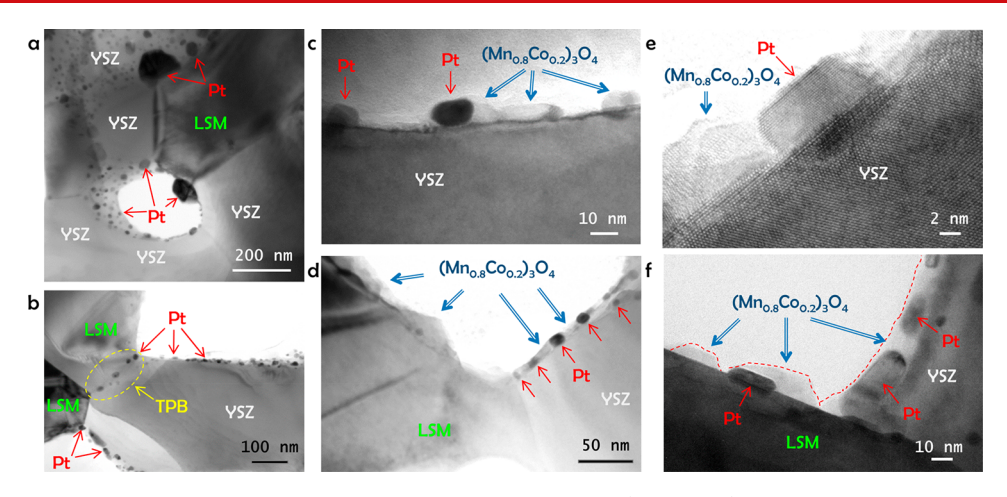


Figure 2. Representative TEM images from cell no. 2 with Pt and the 5 nm thick  $(Mn_{0.8}Co_{0.2})_3O_4$  layer after 24 h of operation. (a) Bimodel distribution of the Pt particles with the larger Pt particles exclusively at the original TPBs. (b) Small Pt particles on YSZ surface and in a plan-view region of an original TPB which is circled. (c) Small Pt particles and discrete  $(Mn_{0.8}Co_{0.2})_3O_4$  particles on the YSZ surface. (d) a Larger island-shaped  $(Mn_{0.8}Co_{0.2})_3O_4$  grains on LSM surface. (e) Faceted Pt particles kept a well-defined orientation relationship with YSZ grain. (f) Small Pt embedded at the interface of LSM/ $(Mn_{0.8}Co_{0.2})_3O_4$  particles that is close to the original TPB. The red dashed lines indicate the surface of the architecture.

afterward (shown in Figure S2a). After 120 h of operation, cell no. 3 exhibits the peak power density of 1.34 W/cm<sup>2</sup> and remains at 305% of the peak power density of that from baseline cell no. 1 (in Figure S2b).

The power density enhancement of ALD coated cells is accompanied by the substantially decreased polarization resistance  $R_n$  with almost unchanged ohmic resistance  $R_s$ , as shown in the Nyquist and Bode plots in Figure 1b,c, and Table 1.  $R_p$  of cell no. 3 is smaller than that of cell no. 2. Furthermore, cell no. 3 features comparable  $R_p$  but much smaller R<sub>s</sub> as compared to the cell no. 4 with LSCF/SDC cathode. To identify the physical origin of the reduced resistance, the dynamic constant in the impedance data is accessed by evaluating the relaxation times and relaxation amplitude of the impedance-related processes using deconvolution.<sup>27-31</sup> Through deconvolution, the distribution of relaxation times (DRT) resolves an impedance spectrum into a higher-resolution plot that allows the identification of individual processes, as shown in Figure 1d. The LSM/YSZ baseline cell exhibits two arcs P1 and P2 with the frequency ranging at 1-4 and 10-200 Hz, respectively, that are largely overlapping each other. By contrast, the ALD-coated cells exhibit two distinct arcs P1 and P2 with much-lowered amplitude. Because the four cells possess identical anode structures and operated under identical conditions, the lowered P1 arc at 1-4 Hz is attributable to changing of gas diffusion and dramatically lower ORR resistance in the cathode.<sup>30</sup> P1 from cell no. 3 is even lower than that of cell no. 4 indicating higher catalytic activity toward ORR than LSCF with mixed conductivity. For the arc P2 at ~70 Hz, the DRTs from cells no. 2 and no. 3 are lower than that of the cell no. 1. It is well agreed in the literature that the physical origin of the arcs that arise at  $\sim$ 70 Hz are primarily due to oxygen transport along the surface and through the bulk in the cathode and YSZ electrolyte. The reduced amplitude of the arc P2 suggests the overall oxygen transport resistance was reduced in cell no. 2 and cell no. 3, in comparison with that of cell no. 1, but higher than that of cell no. 4. In the frequency range higher than 200 Hz, the DRTs from cell no. 3 and LSCF baseline show similar amplitude signifying that oxygen transfer

resistance at the cathode surface in cell no. 3 is nearer to that of the LSCF/SDC cell no. 4.

The above deconvolution analysis revealed that the ORR kinetics and the related electron charge and oxygen mass transfer pathways had been significantly altered in cell no. 2 and cell no. 3 induced by ALD coating. For SOFC, the ORR and oxygen ion transport kinetics are largely affected by the nanostructure of electrode active surfaces that are directly interacting with the reactant gas species. The nanostructure and chemistry of the ALD coated cell no. 2 and no. 3 are thus subjected to transmission electron microscopy (TEM) imaging and analysis. The LSM and YSZ grains, as well as the chemistry of the ALD layer, were confirmed by energy dispersive spectroscopy (EDS) under the TEM.

Representative TEM images (Figure 2) from cell no. 2 illustrate the LSM/YSZ surface structure with Pt and (Mn<sub>0.8</sub>Co<sub>0.2</sub>)<sub>3</sub>O<sub>4</sub> nanograins. Pt particles present a bimodel distribution with the large Pt particles up to ~100 nm exclusively distributed at the original TPB regions (Figure (2a,b) and the very small Pt catalyst particles  $\sim 10$  nm appearing at both the TPBs and on the YSZ surface (Figure 2c-f). Pt particles possess a strongly bonded interface with the YSZ surface, and some of the Pt particles are faceted and have developed well-defined crystal orientation relationship with YSZ grain as shown in Figure 2e. The Pt catalysts are always adjacent to the  $(Mn_{0.8}Co_{0.2})_3O_4$  nanograins that are rectangular shaped with the shorter dimension of  $\sim 5-7$  nm and elongated along the YSZ grain surface (Figure 2c,e,f). By contrast, most of the LSM grain surface is free of Pt, as shown in Figure 2b and Figure S3. Occasionally, in the region that is adjacent to the original TPB region, sparsely distributed Pt grains appear to be embedded at the interface between the  $(Mn_{0.8}Co_{0.2})_3O_4$  and LSM (Figure 2f). Overall, Pt emerged as a selective distribution on YSZ grain surface and not on the LSM surface. Also,  $(Mn_{0.8}Co_{0.2})_3O_4$  grains on LSM are irregularly shaped with a much larger dimension of ~30-50 nm (Figure 2d,e) versus ~10 nm  $(Mn_{0.8}Co_{0.2})_3O_4$  grains on the YSZ surface. The selective ALD deposition of nanoparticles on surfaces of different materials has been reported before. 32,33 However, in terms of the SOFC applications, the

as-deposited ALD Pt layer is conformal on both the LSM and YSZ grain surfaces. <sup>26</sup> In cell no. 2, the selective distribution of Pt occurs upon electrochemical operation at high temperatures.

This phenomenon of selective distribution of Pt particles on YSZ but not on LSM grain surfaces was eliminated in cell no. 3 with the 15 nm thick  $(Mn_{0.8}Co_{0.2})_3O_4$  layer. After electrochemical operation for 120 h, cell no. 3 depicts a conformal and uniform ALD layer with subjacent Pt and superjacent  $(Mn_{0.8}Co_{0.2})_3O_4$  (Figure 3a). Remarkably, the  $(Mn_{0.8}Co_{0.2})_3O_4$ 

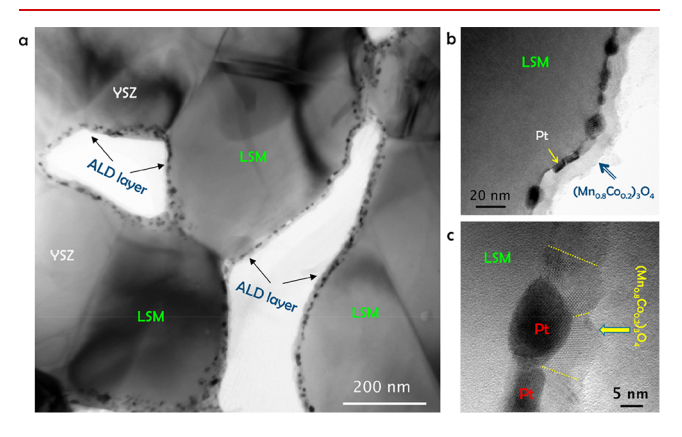


Figure 3. TEM images from the operating cell no. 3 with Pt and then 15 nm thick  $(Mn_{0.8}Co_{0.2})_3O_4$  layer, after 120 h operation. (a) The  $(Mn_{0.8}Co_{0.2})_3O_4$  grains and Pt particles are simultaneously preserved on both the YSZ and LSM grain surface after operation. (b) Small Pt particles with dense and continuous  $(Mn_{0.8}Co_{0.2})_3O_4$  nanoionics on LSM surface. (c) Grain boundaries of the  $(Mn_{0.8}Co_{0.2})_3O_4$  layer are high in density, and the  $(Mn_{0.8}Co_{0.2})_3O_4$  grains and Pt particles are  $\sim 10$  nm.

grains and Pt particles are all  $\sim 10$  nm in dimension, and the Pt particles are simultaneously pinned on both the YSZ and LSM grain surface. Some of the Pt particles are faceted (Figure 3b), featuring a strongly bonded intimate interface with the LSM grain surface (Figure 3c). The  $(Mn_{0.8}Co_{0.2})_3O_4$  superjacent layer presents  $\sim 10$  nm single-layered nanograins with high-density grain boundaries (Figure 3c). The ALD layer also features nanopores (shown in Figure S4), allowing gas penetration.

The internal surface of cathodes with different surface architecture is shown in Figure 4. In comparison with the asreceived commercial cells (Figure 4a) with a bare surface, Figure 4b illustrates the distributions of nanograined Pt and  $(Mn_{0.8}Co_{0.2})_3O_4$  on cathode backbone in cell no. 2, except for Pt  $\sim 100$  nm in a dimension that is too large to fit into the schematic.

The ALD as-deposited Pt is controlled to be an approximately 3 nm discrete crystal sphere. 26 However, in the operated cell no. 2 shown in Figure 2a, some Pt particles were found to be up to ~100 nm in dimension and preferentially accumulate at the original TPB region. The existence of large Pt particles in cell no. 2 indicates that nanosized Pt (not adjacent to the original TPBs) may undergo migration that may be driven by the oxygen partial pressure changes during the electrochemical reactions. According to the diagram of PtO2 partial pressure as a function of oxygen partial pressure,<sup>34</sup> without a current load Pt tends to be oxidized and vaporized as gas species in the air at high temperatures. 35 Once the cathodic polarization is applied, the thermodynamic equilibrium partial pressure of PtO2 is sharply altered at TPBs due to the change of local oxygen partial pressure. The low oxygen partial pressure will result in the reduction of

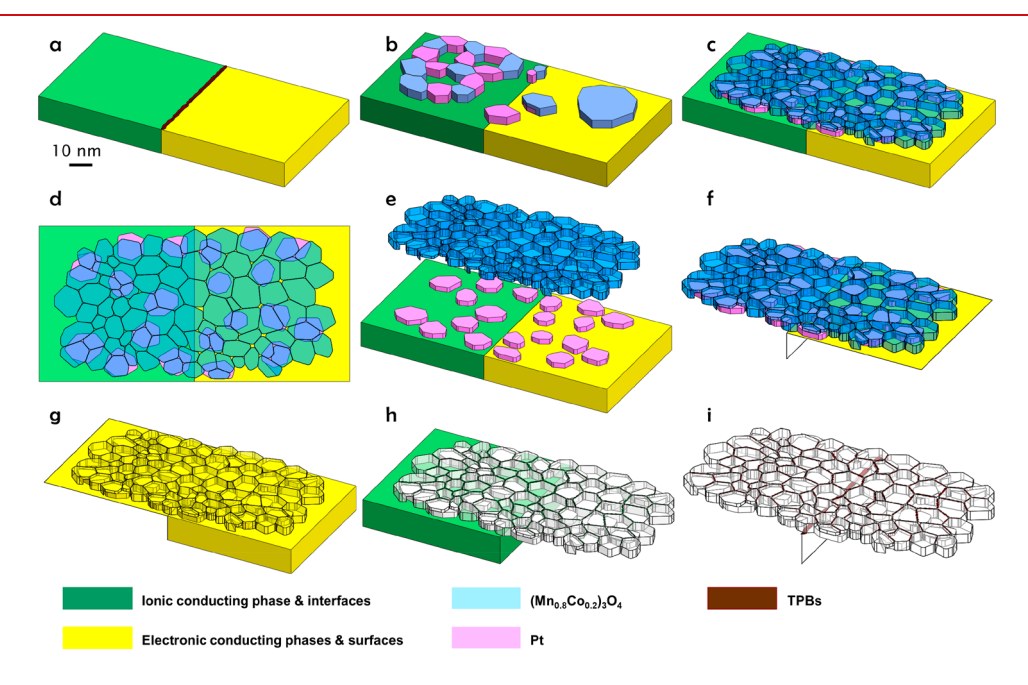


Figure 4. Schematic of the surface architecture on cells no. 1, no. 2, and no. 3. (a) Baseline YSZ/LSM and original TPB. (b) Architecture of  $(Mn_{0.8}Co_{0.2})_3O_4/Pt$  dual layer in cell no. 2. (c) Architecture of  $(Mn_{0.8}Co_{0.2})O_x/Pt$  dual layer in cell no. 3. (d) Top view of ALD layer in cell no. 3. (e) Superjacent  $(Mn_{0.8}Co_{0.2})_3O_4$  nanoionics and subjacent Pt layer respectively in cell no. 3. (f) Distribution of electrocatalyst in cell no. 3. (g) Distribution ionic conductor and ionic conducting interfaces in cell no. 3. (h) Distribution of ionic conductor and ionic conducting interfaces in cell no. 3. (i) Distribution of TPBs in cell no. 3. For all schematics, the ionic conductor is colored in green, the electronic conductor is colored in yellow, the  $(Mn_{0.8}Co_{0.2})O_x$  electrocatalyst is colored in cyan, the Pt is colored in pink, and the electrochemically active sites such as the TPBs are colored in dark red.

**Nano Letters** 

oxidized Pt to metallic Pt at the TPBs, 35,36 likely through reaction 137

$$PtO_{2(g)} + 4e' + 2V''_O \rightarrow Pt_{(s)} + 2O'^{\chi}_O$$
 (1)

where the Pt oxide is reduced by acquiring four electrons, and ionized oxygen subsequently moves away via ionic conductor at TPBs. Such reduction consequently causes the agglomeration of Pt at the original TPBs.

By contrast, much smaller Pt particles of ~10 nm in dimension were also observed uniformly distributed on all YSZ grain surfaces, whereas the well-defined crystal orientation relationship between the slightly elongated Pt nanograins and YSZ (Figure 2e) indicating the reassembly Pt on the YSZ surface. Because the Pt is presumably deposited solely at the TPB region where the oxygen partial pressure is lowered, the uniform distribution on the YSZ surface implies the ALD layer has enabled newly formed TPBs on the YSZ surface, and the YSZ surface possesses both the ionic conductivity and electrical conductivity. Such mixed conductivity on the YSZ in cell no. 2 can be related to the addition of  $(Mn_0 {}_8Co_0 {}_2)_3O_4$ nanograins. First, the reduced Mn cations from the original TPBs and the (Mn<sub>0.8</sub>Co<sub>0.2</sub>)<sub>3</sub>O<sub>4</sub> layer spread out on the YSZ surface, and the Mn-enriched YSZ effectively becomes a mixed conductor and becomes active for direct oxygen incorporation.<sup>38-40</sup> Second, the (Mn<sub>0.8</sub>Co<sub>0.2</sub>)<sub>3</sub>O<sub>4</sub> is an excellent electrocatalyst<sup>41</sup> similar to that of the LSM, and the active electrochemical reaction takes place at the newly formed TPBs of (Mn<sub>0.8</sub>Co<sub>0.2</sub>)<sub>3</sub>O<sub>4</sub>/YSZ/air interface. Upon cell operation, Pt synergistically interacted with (Mn<sub>0.8</sub>Co<sub>0.2</sub>)<sub>3</sub>O<sub>4</sub> and reassembled at (Mn<sub>0.8</sub>Co<sub>0.2</sub>)<sub>3</sub>O<sub>4</sub>/YSZ interface where the oxygen partial pressure is locally lowered during the ORR. The (Mn<sub>0.8</sub>Co<sub>0.2</sub>)<sub>3</sub>O<sub>4</sub> and Pt intimately bonded and alternatively distributed on the YSZ surface as shown in both Figure 2 and Figure 4b. In cell no. 2, there is also a very small amount of Pt nanograins (Figure 2d,f) observed at the LSM/ (Mn<sub>0.8</sub>Co<sub>0.2</sub>)<sub>3</sub>O<sub>4</sub> interface region of ~50 nm to the LSM/ YSZ interface, where the active TPB could be extended through polarization. Except for that, most of the LSM grain surface is free of nano Pt, implying the lack of effective TPBs. The (Mn<sub>0.8</sub>Co<sub>0.2</sub>)<sub>3</sub>O<sub>4</sub> on LSM surface exhibits much bigger grain size than that on the YSZ surface.

In cell no. 3, the as-deposited  $(Mn_{0.8}Co_{0.2})_3O_4$  layer thickness increased to about ~15 nm, which is thick enough to facilitate the formation of continuous layer and connectivity of the neighboring (Mn<sub>0.8</sub>Co<sub>0.2</sub>)<sub>3</sub>O<sub>4</sub> crystal grains. Singlelayered (Mn<sub>0.8</sub>Co<sub>0.2</sub>)<sub>3</sub>O<sub>4</sub> nanograins with the dimension of ~10 nm are well preserved on both the YSZ and LSM grain surface after 120 h cell operation. The salient feature of uniform distribution of nanosized Pt pinned on both the LSM and YSZ grain surface revealed that effective TPBs are covering the entire internal surface of the cathode backbone in cell no. 3. Although the formation mechanisms of TPBs on the YSZ surface is similar to that from cell no. 2, the formation of the TPBs on the LSM surface in cell no. 3 is intriguing. Because LSM is an excellent electrical conductor with negligible ionic conductivity, an additional ionic conducting path on the LSM grain surface is needed to enable the formation of the local TPBs. In cell no. 3, the oxygen ions have four possible pathways for conduction on the LSM surface, namely (i) along the (Mn<sub>0.8</sub>Co<sub>0.2</sub>)<sub>3</sub>O<sub>4</sub> surface boundaries, (ii) along the (Mn<sub>0.8</sub>Co<sub>0.2</sub>)<sub>3</sub>O<sub>4</sub>/LSM interface, (iii) through the LSM and/ or  $(Mn_{0.8}Co_{0.2})_3O_4$  grains, and (iv) along the  $(Mn_{0.8}Co_{0.2})_3O_4$ intergranular grain boundaries. When the surface coating is

single-layered and with grains of constant width of 10 nm and film thickness 10 nm, we could roughly estimate that the grain boundary density of the surface layer in cell no. 3 is significantly high, up to  $\sim 1500~\mu m^{-2.42}$  The high-density surface grain boundaries exposed to air may have played an important role in enhancing the ionic conductivity and accelerating the kinetics of overall surface reactions. 43 There is increasing evidence indicating that the heterostructured interfaces between the oxides (i.e., (Mn<sub>0.8</sub>Co<sub>0.2</sub>)<sub>3</sub>O<sub>4</sub> and LSM) may also facilitate the oxygen ion transport due to the interface strain, space charge effect, and atomic reconstruction at those interfaces. 44,45 Nevertheless, due to the negligible intragranular ionic conductivity of (Mn<sub>0.8</sub>Co<sub>0.2</sub>)<sub>3</sub>O<sub>4</sub> nanograins that are conformal on the LSM surface, the oxygen ions transferring from the  $(Mn_{0.8}Co_{0.2})_3O_4$  surface grain boundaries inevitably pass through the high-density grain boundaries to reach the (Mn<sub>0.8</sub>Co<sub>0.2</sub>)<sub>3</sub>O<sub>4</sub>/LSM interface and facilitate the formation of TPBs. The high-density TPBs on the LSM surface implies the substantial intergranular ionic conductivities through the highdensity grain boundaries of nanograined (Mn<sub>0.8</sub>Co<sub>0.2</sub>)<sub>3</sub>O<sub>4</sub>.

To unambiguously evaluate the intergranular ionic conductivity of the (Mn<sub>0.8</sub>Co<sub>0.2</sub>)<sub>3</sub>O<sub>4</sub> and to exclude the conductivity contribution from the surface grain boundaries, the single-phase bulk scale  $(Mn_{0.8}Co_{0.2})_3O_4$  samples with the grain size of ~200 nm are synthesized. Although the electron block is applied during the conductivity measurement, the nanostructured (Mn<sub>0.8</sub>Co<sub>0.2</sub>)<sub>3</sub>O<sub>4</sub> presents substantial ionic conductivities at 800 and 750 °C which are even within the same order of magnitude of ionic conductors YSZ and samarium-doped cerium oxide, as detailed in Table S1 and Figure S5. This result is in excellent agreement with the density function calculation<sup>46</sup> and our previous experimental evidence regarding LSM<sup>37</sup> clarifying that the grain boundaries from the electrical oxide conductor (Mn<sub>0.8</sub>Co<sub>0.2</sub>)<sub>3</sub>O<sub>4</sub> possess substantial ionic conductivity. The ionic conductivity of the superjacent  $(Mn_{0.8}Co_{0.2})_3O_4$  layer in cell no. 3 is expected to be higher due to the much smaller sized grain and resulted in much higher density grain boundaries. 47 Therefore, the superjacent electrocatalytic (Mn<sub>0.8</sub>Co<sub>0.2</sub>)<sub>3</sub>O<sub>4</sub> layer possesses substantial ionic conductivity and formed the nanoionic network. Such conformal surface architecture enabled the high-density TPBs and further pin the Pt uniformly onto the entire surface of LSM that is dominant with high electrical conductivity.

The surface nanoionics and heterogeneous dual-layer in cell no. 3 are nanoporous allowing reaction gas traveling through the thin ALD layer and accessing the original backbone surface, as shown in Figure S4. On the YSZ backbone, electrocatalyst Pt is sandwiched between the mixed conducting YSZ surface and electrocatalytic (Mn<sub>0.8</sub>Co<sub>0.2</sub>)<sub>3</sub>O<sub>4</sub> nanograins. Once the oxygen is reduced on the gas exposed Pt and gas exposed (Mn<sub>0.8</sub>Co<sub>0.2</sub>)<sub>3</sub>O<sub>4</sub> grain surface, the oxygen ions could quickly diffuse along with the adjacent Pt/YSZ interface,  $(Mn_{0.8}Co_{0.2})_3O_4/YSZ$  interface, as well as the  $(Mn_{0.8}Co_{0.2})_3O_4$ surface grain boundaries, as shown in Figure 4h. On the other hand, three kinds of electrocatalysts, that is, LSM, (Mn<sub>0.8</sub>Co<sub>0.2</sub>)<sub>3</sub>O<sub>4</sub>, and Pt, contribute simultaneously for accelerated ORR on the LSM surface. Meanwhile, there are multiple ionic conduction (Figure 4h) pathways along the (Mn<sub>0.8</sub>Co<sub>0.2</sub>)<sub>3</sub>O<sub>4</sub> surface grain boundaries, (Mn<sub>0.8</sub>Co<sub>0.2</sub>)<sub>3</sub>O<sub>4</sub> intergranular grain boundaries, and LSM/(Mn<sub>0.8</sub>Co<sub>0.2</sub>)<sub>3</sub>O<sub>4</sub> interfaces, that are intimately connected to the electrocatalysts and rapidly transfer the reduced oxygen ion away. The surface nanoionics effectively shifts the mass and charge transfer and

ORR sites from the original TPBs to the entire LSM/YSZ

Nanoionics<sup>48,48,49</sup> hold great promise for SOFCs that incorporate oxygen ionic conducting ceramics in the electrolyte and composite electrodes. Nevertheless, nanoionics and nanostructured electrode<sup>50</sup> development have been very challenging for solid oxide fuel cells (SOFCs) due to poor stability of the nanocrystals during fabrication of SOFCs at elevated temperatures, among other reasons. Following our previous work on the establishment of nanoionics using the ionic conductor of ZrO<sub>2</sub>, the present work demonstrates the formation of the stable and conformal electrocatalytic surface nanoionics that directly enabled the nanostructured electrode that has been constantly pursued yet barely succeeded for practical applications. 51 The very small grain size of  $(Mn_{0.8}Co_{0.2})_3O_4$  in cell no. 3 indicates that the electrical bias applied on the cathode surface and reduced oxygen partial pressure during the high-temperature operation may have favored the possible ion and defects migration primarily along the grain boundaries and achieved the grain retardation within  $(Mn_{0.8}Co_{0.2})_3O_4$  surface nanoionics. <sup>52</sup> The interaction between the dual catalyst and pinning of the nano Pt presented in this study is driven by the sequential catalytic activity from two kinds of electrocatalysts and does not have to be limited by the exact chemistry of catalysts. It thus opens further research directions for electrocatalytic surface nanoionics with a wide range of chemistry and applicable various cathode backbones. The focus of this work is on investigating the versatilities and fundamentals of ALD coating of a minute amount of catalyst on the nanostructure and performance of fuel cells. Upon the establishment of conformal eletrocatalytic nanoionics on the LSM/YSZ backbone, we will carry out the long-term stability test. Such a test would be targeted for ~2000-5000 h of operation to support the expectation of SOFC operation of ~2000 h or above for various portable and stational applications. Furthermore, the conformal electrocatalytic surface nanoionics (Mn<sub>0.8</sub>Co<sub>0.2</sub>)<sub>3</sub>O<sub>4</sub> also potentially offer multifunctionality of mitigating the grain coarsening by cation surface diffusion and increase the cathode chromiumresistance. Spinel (MnCo)<sub>3</sub>O<sub>4</sub> is an excellent interconnecting coating material to seal off the Cr vapor penetration into the cathode backbone<sup>42</sup> and provides the alternative approach of increasing the Cr resistance. We will also investigate the stability of (MnCo)<sub>3</sub>O<sub>4</sub> conformal electrocatalytic surface nanoionics upon exposure to Cr contamination and the electrode thermal cycling.

Summary. For the well-developed SOFC with an LSM/ YSZ cathode, the present work demonstrated that both the high-density nano-electrocatalyst and electrocatalytic nanoionics with high-density grain boundaries could be precisely introduced onto the cathode backbone to simultaneously boost the cell peak power density and specific power by  $\sim$ 350%. The electrocatalytic surface nanoionics from the present study consequently enabled the formation of a nanostructured electrode. This bears an immediate breakthrough on the SOFC technology because the applied ALD processing is scalable to both the single cells and SOFC stacks. Most importantly, the stable and active electrocatalytic surface nanoionics enabled by ALD are with enormous surface area and open new research directions in many electrochemical devices, including both the conventional and protonic conducting SOFCs.

### ASSOCIATED CONTENT

# S Supporting Information

The Supporting Information is available free of charge on the ACS Publications website at DOI: 10.1021/acs.nanolett.9b03515.

Experimental section, Figures S1-S5, Tables S1, and experiment of synthesis and conductivity measurement 

## AUTHOR INFORMATION

## **Corresponding Author**

\*E-mail: xueyan.song@mail.wvu.edu.

ORCID

Xueyan Song: 0000-0002-9878-5883

### Notes

The authors declare no competing financial interest.

# ACKNOWLEDGMENTS

X.S., Y.C., A.H., L.L., and S.P. acknowledges the financial support from DE-FE0023386 and DE-FE 0031251. X.S. acknowledges the support from NSF-DMR 1254594 and NSF-DMR 1916581. Discussions with Dr. Harry Finklea at West Virginia University, regarding the principle of SOFC impedance deconvolution, is greatly appreciated.

### REFERENCES

- (1) Irvine, J. T.; Neagu, D.; Verbraeken, M. C.; Chatzichristodoulou, C.; Graves, C.; Mogensen, M. B. Nature Energy 2016, 1, 15014.
- (2) Myung, J.-h.; Neagu, D.; Miller, D. N.; Irvine, J. T. Nature 2016, 537, 528.
- (3) Sengodan, S.; Choi, S.; Jun, A.; Shin, T. H.; Ju, Y.-W.; Jeong, H. Y.; Shin, J.; Irvine, J. T.; Kim, G. Nat. Mater. 2015, 14, 205.
- (4) Chen, Y.; deGlee, B.; Tang, Y.; Wang, Z.; Zhao, B.; Wei, Y.; Zhang, L.; Yoo, S.; Pei, K.; Kim, J. H.; et al. Nature Energy 2018, 3,
- (5) Choi, S.; Kucharczyk, C. J.; Liang, Y.; Zhang, X.; Takeuchi, I.; Ji, H.-I.; Haile, S. M. Nature Energy 2018, 3, 202.
- (6) Duan, C.; Kee, R. J.; Zhu, H.; Karakaya, C.; Chen, Y.; Ricote, S.; Jarry, A.; Crumlin, E. J.; Hook, D.; Braun, R.; et al. Nature 2018, 557,
- (7) Kendall, K.; Kendall, M. High-temperature solid oxide fuel cells for the 21st century: fundamentals, design and applications; Elsevier, 2015.
- (8) Boldrin, P.; Brandon, N. P. Nature Catalysis 2019, 2, 571.
- (9) Minh, N. Q.; Mogensen, M. B. Electrochem. Soc. Interface 2013, 22, 55-62.
- (10) Ebbesen, S. D.; Mogensen, M. J. Power Sources 2009, 193, 349-
- (11) Shim, J. H. Nature Energy 2018, 3, 168.
- (12) Minh, N. Q. J. Am. Ceram. Soc. 1993, 76, 563-588.
- (13) Adler, S. B. Chem. Rev. 2004, 104, 4791-4843.
- (14) Sholklapper, T. Z.; Radmilovic, V.; Jacobson, C. P.; Visco, S. J.; De Jonghe, L. C. J. Power Sources 2008, 175, 206-210.
- (15) Druce, J.; Téllez, H.; Hyodo, J. MRS Bull. 2014, 39, 810-815.
- (16) Ding, D.; Li, X.; Lai, S. Y.; Gerdes, K.; Liu, M. Energy Environ. Sci. 2014, 7, 552-575.
- (17) Vohs, J. M.; Gorte, R. J. Adv. Mater. 2009, 21, 943-956.
- (18) Shah, M.; Voorhees, P. W.; Barnett, S. A. Solid State Ionics 2011, 187, 64-67.
- (19) Knofel, C.; Wang, H. J.; Thyden, K. T. S.; Mogensen, M. Solid State Ionics 2011, 195, 36-42.
- (20) Song, X.; Lee, S.; Chen, Y.; Gerdes, K. Solid State Ionics 2015, 278, 91-97.
- (21) Onn, T.; Küngas, R.; Fornasiero, P.; Huang, K.; Gorte, R. Inorganics 2018, 6, 34.

(22) O'Neill, B. J.; Jackson, D. H.; Lee, J.; Canlas, C.; Stair, P. C.; Marshall, C. L.; Elam, J. W.; Kuech, T. F.; Dumesic, J. A.; Huber, G. W. ACS Catal. 2015, 5, 1804–1825.

- (23) Chao, C.-C.; Motoyama, M.; Prinz, F. B. Adv. Energy Mater. **2012**, *2*, 651–654.
- (24) Choi, H. J.; Bae, K.; Grieshammer, S.; Han, G. D.; Park, S. W.; Kim, J. W.; Jang, D. Y.; Koo, J.; Son, J. W.; Martin, M.; et al. *Adv. Energy Mater.* **2018**, *8*, 1802506.
- (25) Chen, Y.; Hinerman, A.; Liang, L.; Gerdes, K.; Navia, S. P.; Prucz, J.; Song, X. J. Power Sources 2018, 405, 45–50.
- (26) Chen, Y.; Gerdes, K.; Song, X. Sci. Rep. 2016, 6, 32997.
- (27) Leonide, A.; Ruger, B.; Weber, A.; Meulenberg, W. A.; Ivers-Tiffee, E. J. Electrochem. Soc. **2010**, 157, B234–B239.
- (28) Kornely, M.; Menzler, N.; Weber, A.; Ivers-Tiffée, E. Fuel Cells **2013**, 13, 506–510.
- (29) Sonn, V.; Leonide, A.; Ivers-Tiffée, E. J. Electrochem. Soc. 2008, 155, B675–B679.
- (30) Liu, B.; Muroyama, H.; Matsui, T.; Tomida, K.; Kabata, T.; Eguchi, K. J. Electrochem. Soc. 2010, 157, B1858–B1864.
- (31) Barfod, R.; Mogensen, M.; Klemenso, T.; Hagen, A.; Liu, Y.-L.; Vang Hendriksen, P. J. Electrochem. Soc. 2007, 154, B371.
- (32) Xie, J.; Yang, X.; Han, B.; Shao-Horn, Y.; Wang, D. ACS Nano 2013, 7, 6337-6345.
- (33) Xie, J.; Liao, L.; Gong, Y.; Li, Y.; Shi, F.; Pei, A.; Sun, J.; Zhang, R.; Kong, B.; Subbaraman, R.; Christensen, J.; Cui, Y. Science advances 2017, 3, No. eaao3170.
- (34) Shin, S. M.; Yoon, B. Y.; Kim, J. H.; Bae, J. M. Int. J. Hydrogen Energy 2013, 38, 8954–8964.
- (35) Xiong, Y.; Yamaji, K.; Kishimoto, H.; Brito, M. E.; Horita, T.; Yokokawa, H. Electrochem. Solid-State Lett. 2009, 12, B31–B33.
- (36) Chen, Y.; Liang, L.; Paredes Navia, S. A.; Hinerman, A.; Gerdes, K.; Song, X. ACS Catal. 2019, 9, 6664–6671.
- (37) Simner, S. P.; Anderson, M. D.; Pederson, L. R.; Stevenson, J. W. J. Electrochem. Soc. **2005**, 152, A1851.
- (38) Backhaus-Ricoult, M. Solid State Ionics 2006, 177, 2195-200.
- (39) Backhaus-Ricoult, M.; Adib, K.; Clair, T. S.; Luerssen, B.; Gregoratti, L.; Barinov, A. Solid State Ionics 2008, 179, 891-895.
- (40) Nielsen, J.; Mogensen, M. Solid State Ionics 2011, 189, 74-81.
- (41) Liu, H.; Zhu, X.; Cheng, M.; Cong, Y.; Yang, W. Chem. Commun. 2011, 47, 2378–2380.
- (42) Kumar, R.; Nicola, L.; Van der Giessen, E. Mater. Sci. Eng., A 2009, 527, 7-15.
- (43) An, J.; Shim, J. H.; Kim, Y.-B.; Park, J. S.; Lee, W.; Guer, T. M.; Prinz, F. B. *MRS Bull.* **2014**, *39*, 798–804.
- (44) Lee, S.; MacManus-Driscoll, J. L. APL Mater. 2017, 5, 042304.
- (45) Mayeshiba, T.; Morgan, D. Phys. Chem. Chem. Phys. 2015, 17, 2715-2721.
- (46) Polfus, J. M.; Yildiz, B.; Tuller, H. L. Phys. Chem. Chem. Phys. **2018**, 20, 19142–19150.
- (47) Sata, N.; Eberman, K.; Eberl, K.; Maier, J. Nature 2000, 408, 946-949.
- (48) Maier, J. Solid State Ionics 2002, 148, 367-374.
- (49) Maier, J. Nat. Mater. 2005, 4, 805-815.
- (50) Wachsman, E. D.; Lee, K. T. Science 2011, 334, 935-939.
- (51) Lee, K. T.; Wachsman, E. D. MRS Bull. 2014, 39, 783-791.
- (52) Munir, Z. A.; Quach, D. V.; Ohyanagi, M. J. Am. Ceram. Soc. **2011**, 94, 1–19.